RSC Advances

ROYAL SOCIETY OF CHEMISTRY

www.rsc.org/advances

Journal Name

ARTICLE

Preparation and enhanced photoelectrochemical performance of p-n heterojunction $CuFe_2O_4/WO_3$ nanocomposite film

Received 00th January 20xx,
Accepted 00th January 20xx

DOI: 10.1039/x0xx00000x

www.rsc.org/

Yang Liu[1], Haizhou He[1], Jie Li[1], Wenzhang Li[1,*], Yahui Yang[2], Yaomin Li [3], Qiyuan Chen[1]

In this work, a p-n heterojunction film consisting of n-type WO_3 and p-type $CuFe_2O_4$ was synthesized via two steps. The n-type WO_3 film was deposited on the FTO substrate by a doctor-blade method and then modified with p-type $CuFe_2O_4$ nanoparticles by a deposition-annealing method. The composite film was characterized by X-ray powder diffraction, scanning electron microscopy, transmission electron microscopy, X-ray photoelectron spectroscopy and UV-vis diffuse reflectance spectroscopy, showing that the $CuFe_2O_4$ nanoparticles were deposited on the surface of WO_3 film. Meanwhile, photoelectrochemical measurements were used to investigate the photoelectrochemical properties. A photocurrent of 0.75 mA/cm^2 at 0.6 V (vs. Ag/AgCl) was achieved with $CuFe_2O_4/WO_3$, resulting in a 2.68 fold increase compared to pristine WO_3. The presence of p-n heterojunction facilitates the separation of photoinduced electrons and holes, leading to more efficient charge transfer, resulting in a significant improvement in PEC performance.

1. Introduction

To solve the severe energy crisis and environmental pollution issues caused by the excessive consumption of traditional fossil fuels (coal, crude oil and natural gas) in the past decades, a lot of research has been reported. Among them, photoelectrochemical (PEC) water splitting, as an efficient, green and promising approach to generate renewable energy from sunlight, has triggered enormous research activities since Honda and Fujishima's report [1]. To date, various kinds of semiconductor materials have been synthesized and investigated [2, 3]. Because of its photosensitivity, chemical stability and environmental friendliness, tungsten trioxide (WO_3) has been regarded as one of the ideal materials for solar-driven water splitting [4].

Even though WO_3 has these promising characteristics, further improving the photoelectrochemical performance is necessary in order to satisfy practical application requirements. Besides loading WO_3 on the conductive substrates (FTO or ITO) is in favor of the reuse and recycle of photocatalyst, most of the researchers have focused on broadening the photoresponse region of semicondutor or improving the separation of the photo-generated electrons and holes [5-7]. The main methods for achieving the goal have included noble metal deposition [8, 9], metal or non-metal element doping [5, 6, 10, 11], surface modification [12], or coupled with other semiconductors [13-18]. Among them, coupled with other semiconductors, which can promote the separation of the photoinduced electron-hole pairs via the different position of valence and conduction band from each other, is an effective method to improve the efficiency of water splitting.

MFe_2O_4 (M = Cu, Zn, Co et.al), which is a high thermal stable material with effective catalytic activity, has been used extensively in photocatalysis and solar water-splitting [19-21]. Since most of the ferrates are p-type semiconductors, some of them can couple with n-type semiconductors to form p-n heterojunction composite particles ($CuFe_2O_4$/CdS, $CuFe_2O_4/SnO_2$, $CuFe_2O_4/TiO_2$ and $CaFe_2O_4/WO_3$) [14, 22-24]. For example, Miyauchi et al. prepared $CaFe_2O_4/WO_3$ composite powders by mechanically mixing n-type WO_3 with p-type $CaFe_2O_4$ particles, and the composite photocatalyst showed better performance than WO_3 on the photocatalytic decomposition of acetaldehyde [14]. The enhanced photocatalysis activity can be ascribed to the separation of the photo-generated electron-hole pairs by their potential difference at the p-n heterojunction. Even though the powdered composite photocatalyst is a great candidate in photocatalysis, its application is limited due to the low recyclability. To cover the shortage, loading p-type ferrate on the surface of n-type semiconductor film is expected to be an efficient route. Even though several works on the photocatalysis or photoelectrochemical property of n-type semi-conductor with p-type semiconductor (ferrate [25, 26], Cu_2O [27-30], NiO [31], Si [32], CdTe [33] and BiOI [34] et.al) film have been reported, the n-type WO_3 film loaded with ferrate is lack of attention. To the best of our knowledge, this is the first report to

[1] School of Chemistry and Chemical Engineering, Central South University, Changsha 410083, China

[2] College of Resources and Environment, Hunan Agricultural University, Changsha 410128, China

3 Department of Chemistry, University College London, 20 Gordon Street, London, WC1H 0AJ, UK

*Corresponding author. Tel.: +86 731 8887 9616; fax: +86 731 8887 9616.

E-mail addresses: liwenzhang@csu.edu.cn

Electronic Supplementary Information (ESI) available: [details of any supplementary information available should be included here]. See DOI: 10.1039/x0xx00000x

study the photoelectrochemical performance of WO_3 film loaded with $CuFe_2O_4$ nanoparticles.

In this paper, we fabricated the $CuFe_2O_4/WO_3$ p-n heterojunction film by doctor-blade method and deposition-annealing method. Meanwhile, the photoelectrochemical properties had been systematically characterized by several methods, including linear sweep voltammetry, electrochemical impedance spectroscopy (EIS), Mott–Schottky and incident photon to current conversion efficiency (IPCE).

2. Experimental

2.1 Preparation of $CuFe_2O_4/WO_3$ heterojunction film

All chemicals were analytical grade and were used without further purification. In a typical synthesis, the WO_3 spherical nanopowders were prepared by a solution method [35]. Then, 0.175 g obtained WO_3 nanopowders were added to an agate jar with terpineol (0.8 mL) as a solvent. PEG20000 (0.05 g) and ethylcellulose (0.025 g) were added to the agate jar as additive. Besides, 0.2 mL acetylacetone and 0.2 mL triton were also added to the agate jar. The WO_3 paste was acquired after Ball Milling for 8 h. The WO_3 films were fabricated by the doctor blade method on the FTO glass substrates that had been cleaned up. Finally, the as-prepared WO_3 films were calcined at 450 ℃ for 0.5 h.

A deposition-annealing method was used to synthesize the $CuFe_2O_4$ nanoparticles on the as-prepared WO_3 film (1.5 cm × 1 cm). In detail, 0.060 g of $Cu(CH_3COO)_2 \cdot H_2O$ was dissolved into 10 mL of de-ionized (DI) water to form a transparent solution firstly (solution A). Then, 0.196 g of $K_3Fe(CN)_6$ was dissolved into another 30 mL of DI water to form a transparent solution (solution B). After the two solutions were stirred for 10 min in the ice bath, respectively, the solution A was added into the solution B drop by drop under vigorously stirred in the ice bath. After further stirred in the ice bath for another 1 h, the as-prepared WO_3 film was put into the solution. The mixture was transferred into a refrigerator, keeping at 0-4 °C in a refrigerator for 2 h. Then the film was taken out and washed by dipping in the DI water for 30 seconds. After drying at 60 ℃, the $CuFe_2O_4/WO_3$ film was calcined at 500 ℃ for 1h. For comparison, the pristine WO_3 film and the mixed solution were also calcined to prepare pure WO_3 and bare $CuFe_2O_4$, respectively.

2.2 Characterization

The phase formations of the as prepared films were determined by an X-ray diffractometer (D/Max2250). The morphology of the materials was studied with a field emission scanning electron microscope (FESEM, NanoSEM 230) equipped with an Energy Dispersive X-ray (EDX) analyzer and a transmission electron microscope (TEM, TECNAI G2 F20). The surface elemental analysis was carried out by an X-ray photoelectron spectroscopy (XPS, ESCALAB 250Xi). UV−vis spectra were determined using a UV−vis spectrophotometer (UV-vis, PGeneral TU-1901) in diffuse reflectance mode.

2.3 Photoelectrochemical measurements

The PEC performance of films was characterized by a typical three-electrode electrochemical cell with an electrochemical analyzer (Zennium, Zahner, Germany), using an Ag/AgCl (saturated KCl) reference electrode and a platinum counter electrode. A 0.2 M Na_2SO_4 aqueous solution was used as electrolyte for all of photoelectrochemical tests. Photocurrent−potential plots were characterized by linear sweep voltammogram at 20 mV/s under AM 1.5G illumination, and the scanned range was from 0 to 1.0 V (vs. Ag/AgCl). The electrochemical impedance spectra (EIS) were recorded at 0.3 V (vs. Ag/AgCl) with a 10 mV AC voltage perturbation, and the frequency were varied from 10,000 to 0.1 Hz. Additionally, incident photon to electron conversion efficiency (IPCE) of the film was obtained as a function of wavelength from 310 to 700 nm, and the absolute intensity of the monochromic incident light was measured by a silicon photodiode.

3. Results and discussion

The XRD patterns of WO_3 and $CuFe_2O_4/WO_3$ films are shown in Fig.1. It can be easily seen that the XRD pattern of each sample matchs well with the standard monoclinic phase WO_3 (JCPDS no. 83-0950). Moreover, there are also some peaks corresponding to tetragonal SnO_2 (JCPDS no.46-1088), meaning that the samples were loaded on the FTO substrate. The XRD pattern of the bare $CuFe_2O_4$ was also measured as shown in Fig. S1. The peaks at 2θ values of 18.32, 30.18, 35.60 and 37.10 ° can be indexed to (111) (220) (311) and (222) crystal planes of $CuFe_2O_4$ (JCPDS no. 77-0010). However, typical peaks of $CuFe_2O_4$ or other materials are not observed in $CuFe_2O_4/WO_3$ (Fig.1), which indicates that the concentration of $CuFe_2O_4$ is too low to be detected by XRD.

The SEM images of the WO_3 and $CuFe_2O_4/WO_3$ films are presented in Fig. 2. In Fig.2a and 2b, the top-view of SEM images exhibit that both samples are nanoporous network composed of spherical particles, which are agglomerate and interconnected each other. As can be seen in the cross sectional images (Fig. 2c and 2d), the thickness of both WO_3 and $CuFe_2O_4/WO_3$ films are about 3.2 μm however, the layer of $CuFe_2O_4$ can not be found. It means that $CuFe_2O_4$ may

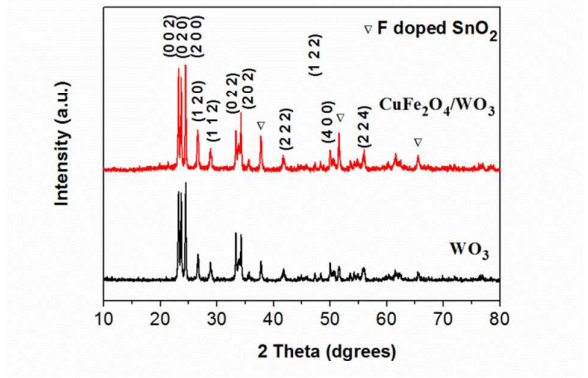

Fig.1 XRD patterns of WO_3 and $CuFe_2O_4/WO_3$ films

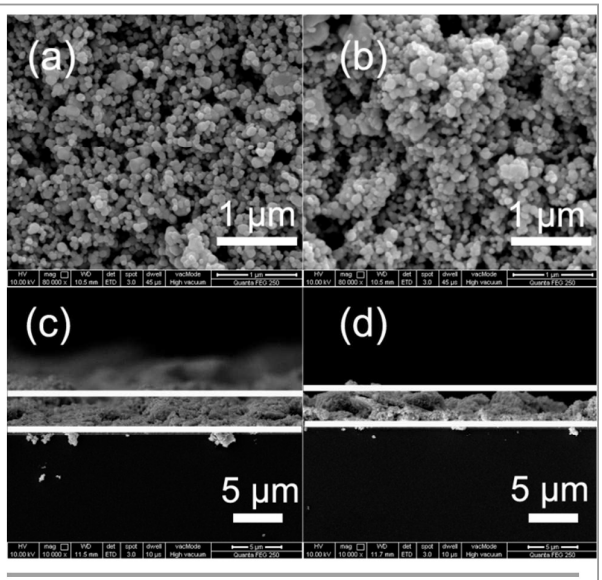

Fig. 2 SEM images of the surface morphology of (a) WO_3 and (b) $CuFe_2O_4/WO_3$ films; cross-sectional micrographs of (c) WO_3 and (d) $CuFe_2O_4/WO_3$ films

compactly deposit on the surface of WO_3 film. Furthermore, the energy dispersive X-ray (EDX) analyses were recorded as shown in the Fig. S2, and Cu and Fe can be detected in the sample of $CuFe_2O_4/WO_3$ (Fig. S2b).

To get more detailed information on the crystalline structure of the composite, the TEM images of $CuFe_2O_4/WO_3$ at different magnifications are displayed in Fig. 3. The low resolution image (Fig. 3a) shows the particles are spheres that are highly agglomerated, and the size of the sphere is approximately 40 nm. It can also be seen that a smaller particle with irregular size adhere to the sphere. Fig. 3b displays the lattice fringes of the smaller particle and sphere. The interplanar distances observed in the smaller particle and the sphere are 0.254 and 0.365 nm, which correspond to the 311- and 200-planes of tetragonal $CuFe_2O_4$ and monoclinic WO_3, respectively. It is proved that $CuFe_2O_4$ nanoparticles are attaching to the WO_3 to form $CuFe_2O_4/WO_3$ composite.

The presence of $CuFe_2O_4$ on the surface of WO_3 film was further confirmed by the XPS spectra (Fig.4). In Fig.4a, the survey spectrum of WO_3 and $CuFe_2O_4/WO_3$ indicates peaks of elements W and O. The carbon peak is attributed to adventitious hydrocarbon from the XPS instrument itself, which is not indicated in the Figure. Fig. 3b shows the XPS spectrum of the tungsten core level (W 4f). The two peaks at 35.47 and 37.62 eV in the spectrum can be assigned to W $4f_{7/2}$ and W $4f_{5/2}$, respectively, which are consistent with the reported values [36]. Fig.4c and 4d show the high-resolution XPS spectra for Fe 2p and Cu 2p, respectively. From the Fe 2p spectrum, it was found that the peaks at 711.2 and 724.7 eV are from Fe 2p3/2 and Fe 2p1/2, and two accompanying satellite peaks visible at binding energies of around 718.4 eV is indicative of the presence of Fe^{3+} cations [37]. Two distinct and intense peaks were appeared for the Cu 2p spectrum, which are Cu 2p3/2 = 932.6 eV and Cu 2p1/2 = 952.4 eV (ΔBE = 19.8 eV) [38]. A satellite peak at about 942.0 eV can also be seen, which provides evidence for the presence of Cu^{2+} [37]. The ICP analysis was employed to determine the concentration of various metals (Cu, Fe and W), and [Cu]:[Fe]:[W] value of 1.51:3.12:100 was estimated, so the ratio of p semiconductor to n semiconductor is about 1.51:100 in our system.

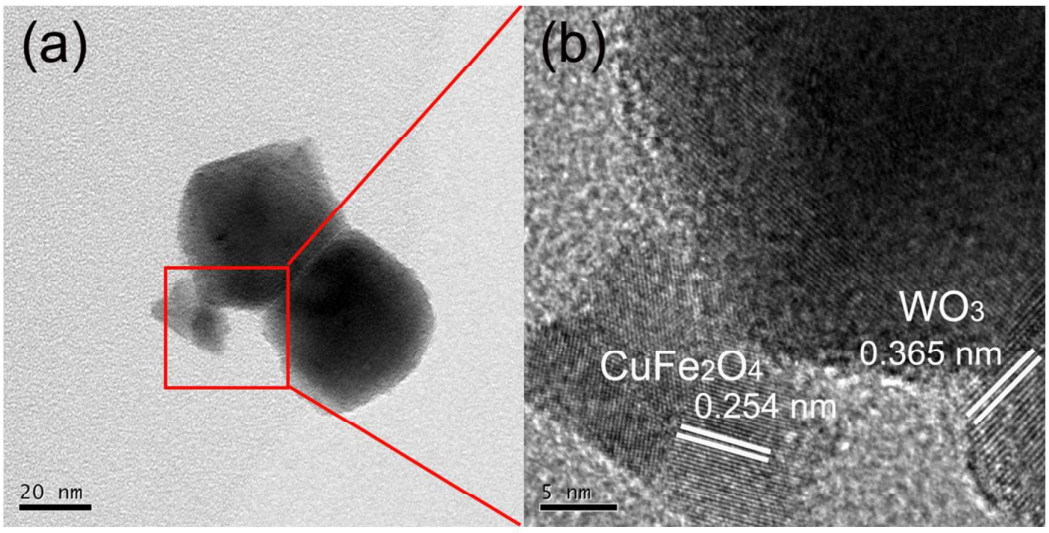

Fig. 3 (a) Transmission electron micrographs and (b) High resolution TEM (HRTEM) image of $CuFe_2O_4/WO_3$

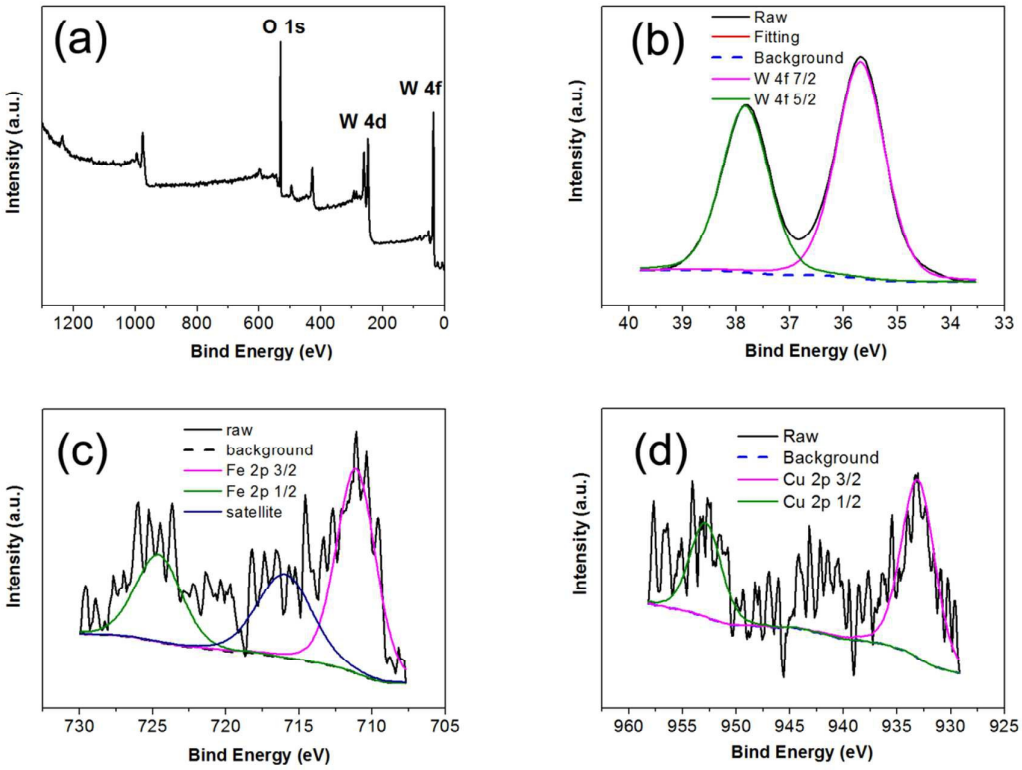

- Fig.4 XPS of $CuFe_2O_4/WO_3$ (a) full spectrum; (b) W 4f; (c) Fe 2p and (d) Cu 2p.

The UV-visible spectra of pure WO_3 and $CuFe_2O_4/WO_3$ films are presented in Fig.5. The bare WO_3 film absorbs light with wavelengths smaller than 455 nm, corresponding to 2.72 eV of band gap energy [39]. The absorbance edge of $CuFe_2O_4/WO_3$ is 463 nm, corresponding to 2.68 eV of band gap energy. The slightly shift of absorbance edge is probably due to the higher absorption coefficient of $CuFe_2O_4$ for visible light (Fig.S3). To investigate the flat band potential (V_{fb}) of samples, Mott-Schottky plots were employed with a frequency of 500 Hz as shown in Fig. 6. The value of V_{fb} is approximately equal to the value of x-intercept, which are 0.08 and 0.19 V (vs. Ag/AgCl) for WO_3 and $CuFe_2O_4/WO_3$, respectively. It can be found that a positive shift of flat band potential, and a shift of the Fermi level to positive potential. It is because that $CuFe_2O_4$

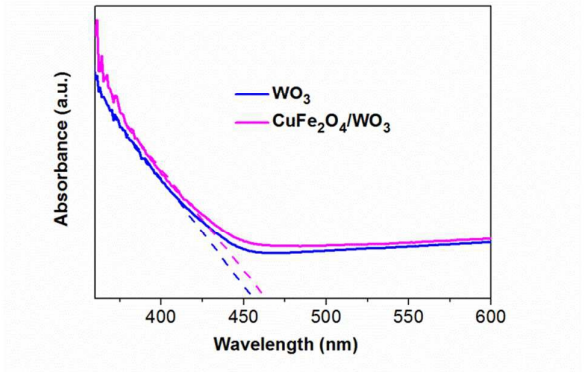

Fig.5 UV-Vis absorbance spectroscopy of the WO_3 and $CuFe_2O_4/WO_3$

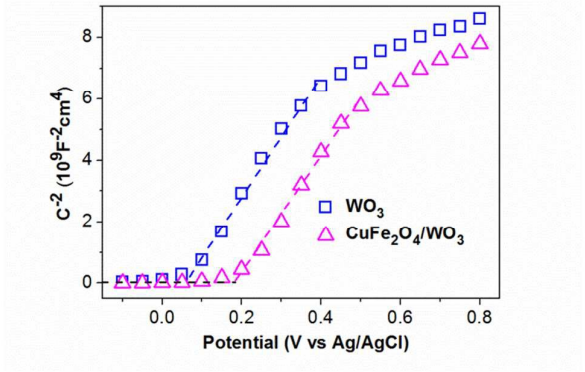

Fig.6 Mott−Schottky plots of the WO_3 and $CuFe_2O_4/WO_3$

is a p-type semiconductor with a negative slope, whose flat band potential is about 0.5 V (vs. Ag/AgCl) (Fig.S4) [31]. Moreover, the potential of Fermi levels of WO_3 and $CuFe_2O_4$ is in equilibrium after forming the p-n heterojunction [24]. So the $CuFe_2O_4/WO_3$ has a positive flat band potential compared with pure WO_3 film.

To further study the effect of the valence band maximum (VBM) of the WO_3 and $CuFe_2O_4/WO_3$, the valence band X-ray photoelectron spectroscopy (VB XPS) was employed to determine the electronic structure. Fig. 7 indicates that the VBM of $CuFe_2O_4/WO_3$ moves to higher potential compared with that of WO_3. That is to say, the VBM of the WO_3 changes after coupling with $CuFe_2O_4$, in agreement with the changing of flat band potential.

To investigate the photoresponsivity of the films, the photocurrent−potential was measured using a linear sweep voltammetry method as shown in Fig.8. The current values of two samples are about zero under dark condition. In the range of 0.3-1.0 V (vs. Ag/AgCl), a significant improvement of photocurrent under irradiation indicates the enhanced PEC activity after loading of $CuFe_2O_4$. A photocurrent of 0.75 mA/cm^2 (0.6 V vs. Ag/AgCl) was achieved with $CuFe_2O_4/WO_3$, which is 1.68 times higher than that of bare WO_3 (0.28 mA/cm^2), The conversion efficiency is about 0.48 % (Fig.S5), and it is higher than the results reported in the similar system [35, 40]. For a semiconductor thin film photoanode, the magnitude of photocurrent is determined by the competition of photo-generated carriers migration and recombination [41]. At the same time, most of the photogenerated electron/hole pairs recombine generating heat and/or light after excitationg [42]. In fact, p-n junction can greatly enhance the charge separation owing to the internal electric field [43]. Hence, the p-n heterojunction formed by n-type WO_3 and p-type $CuFe_2O_4$ has a beneficial effect on the separation of the photo-generated carriers and decreasing the recombination of electrons and holes. In addition, the onset potential of $CuFe_2O_4/WO_3$ (Fig.S6) shows a positive shift compared with pure WO_3, which is consistent with the results of flat band potentials in Fig.6a. To observe the effect of composition (ratio of p/n) on the photoelectrochemical performance, various composite films were fabricated by changing the concentration of $Cu(CH_3COO)_2 \cdot H_2O$ and $K_3Fe(CN)_6$ (the details in the supporting information), and the photocurrent curves are shown in Fig.S7. It can be concluded that the ratio of p/n ≈ 1.51:100 might be the optimized composition in our system. Transient photocurrent were also measured at 0.4 V (vs. Ag/AgCl) with chopped light, as shown in Fig.6b. The photocurrent of both samples are about zero when the light is chopped, and the photocurrent show decay mode under irradiation, meaning that the recombination process occurs. The transient time constant (τ_{tran}) were calculated from the equation: $\exp(-t/\tau_{tran}) = (I_t-I_f)/(I_i-I_f)$ [44, 45]. It is 3.5s for WO_3 and 4.5s for $CuFe_2O_4/WO_3$, respectively, indicating the p-n heterojunction accelerates the separation of photoinduced electrons and holes. The stability of WO_3 and $CuFe_2O_4/WO_3$ were also investigated, as shown in Fig.S8. After irradiation of 1140 s, the photocurrents of WO_3 and $CuFe_2O_4/WO_3$ decrease with 64.1% (from 0.100 to 0.036 mA/cm^2) and 56.2% (from 0.442 to 0.194 mA/cm^2), respectively. It means that the $CuFe_2O_4/WO_3$ film shows a little better stability compared to the bare WO_3 film.

EIS measurement was employed to study the electron transfer resistance across the electrode-electrolyte interfaces under visible irradiation. Fig.9a shows the Nyquist plots which can be used to characterize the charge transfer resistance and

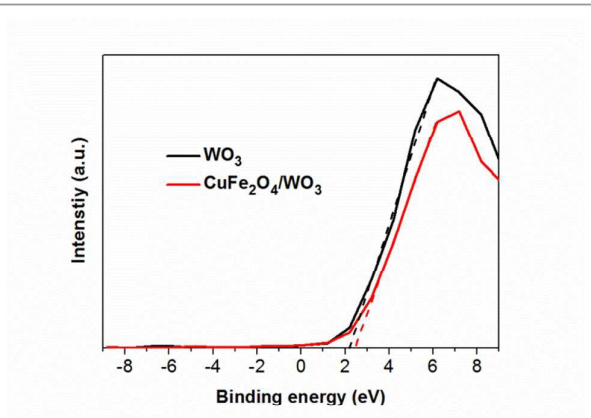

Fig.7 VB-XPS spetra of WO_3 and $CuFe_2O_4/WO_3$

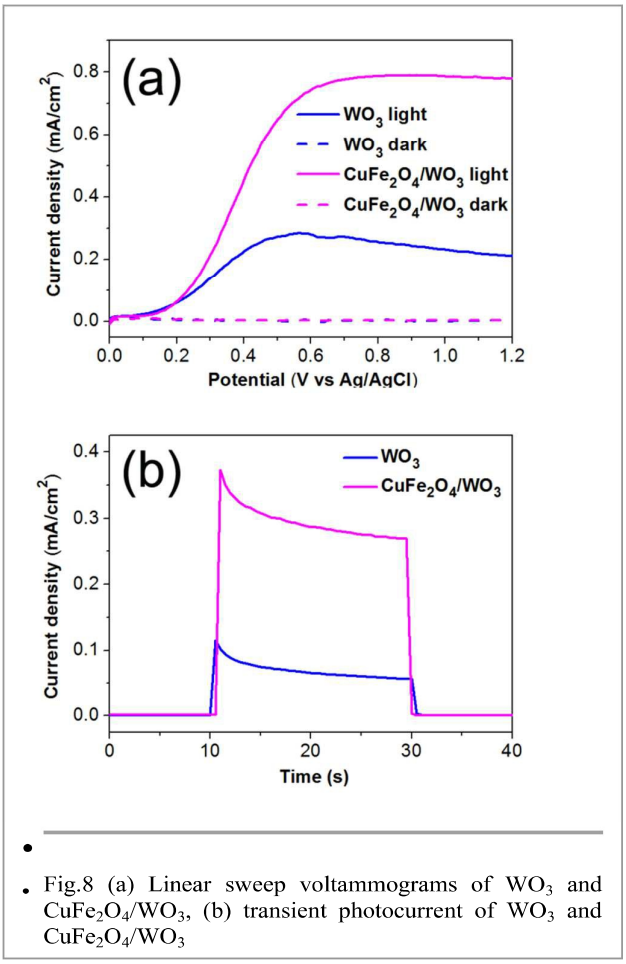

Fig.8 (a) Linear sweep voltammograms of WO_3 and $CuFe_2O_4/WO_3$, (b) transient photocurrent of WO_3 and $CuFe_2O_4/WO_3$

the separation efficiency of the photo-generated electrons and holes [45]. The impedance spectra, consisting of a semicircle, can be fitted with an appropriate equivalent circuit. As shown in Fig.9b, the equivalent circuit includes a series resistance (R_s), a charge transfer resistance (R_{ct}) and a constant phase element (*CPE*). The semicircle of $CuFe_2O_4/WO_3$ is smaller than that of WO_3, and the fitting results of R_{ct} are 2479 and 364 ohm for WO_3 and $CuFe_2O_4/WO_3$, respectively. It means that the p-n heterojunction decrease the charge transfer resistance at the interface of electrode and electrolyte, leading to more efficient charge separation. Correspondingly, the characteristic frequency peaks for WO_3 and $CuFe_2O_4/WO_3$ in Bode phase plots are shown in Fig.9c. The peak of $CuFe_2O_4/WO_3$ shifts to low frequency from 53.5 Hz to 10.0 Hz compared with WO_3. Therefore, the lifetime of photoelectrons (τ) for the films can be estimated by the equation: $\tau=1/2\pi f_{max}$ [45], where f_{max} is the peak frequency, and the τ are 3.0 and 15.9 ms for WO_3 and $CuFe_2O_4/WO_3$, respectively. The presence of p-n heterojunction facilitates the separation of photoinduced electrons and holes, leading to prolongation of photoelectrons lifetime, resulting in a significant improvement in PEC performance.

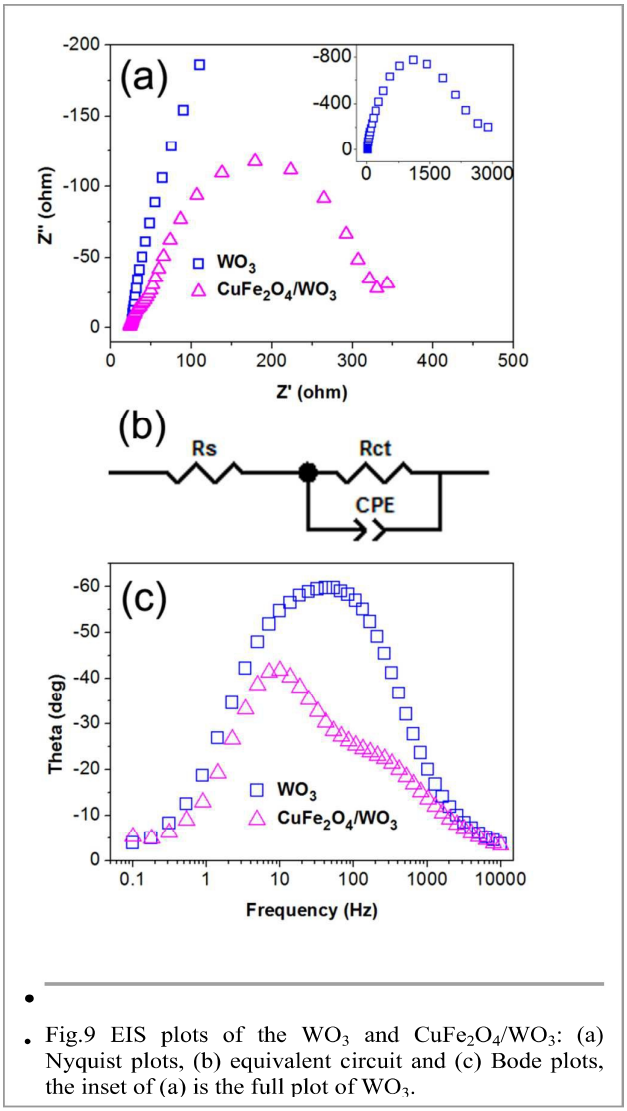

Fig.9 EIS plots of the WO_3 and $CuFe_2O_4/WO_3$: (a) Nyquist plots, (b) equivalent circuit and (c) Bode plots, the inset of (a) is the full plot of WO_3.

In order to further explore the quantitative correlation of light absorption on the films, IPCE measurements were performed at

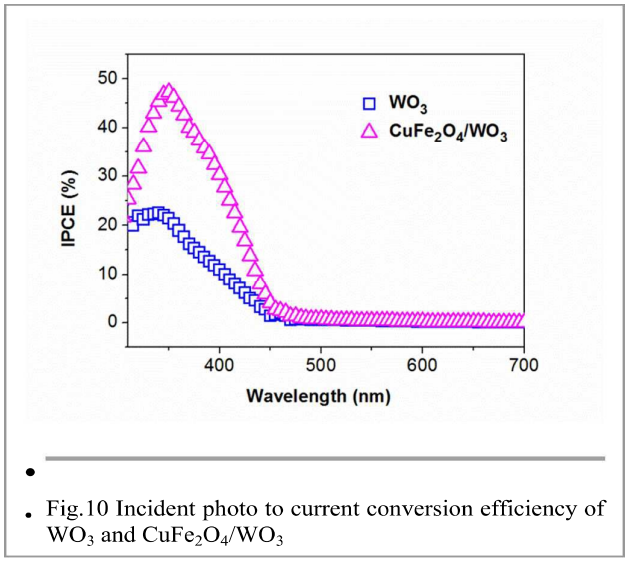

Fig.10 Incident photo to current conversion efficiency of WO_3 and $CuFe_2O_4/WO_3$

the bias of 1.0 V (Fig. 10). The light response region of WO_3 and $CuFe_2O_4/WO_3$ are both at 310-475 nm. The $CuFe_2O_4/WO_3$ film shows a higher IPCE value compared with WO_3 film in the whole photoresponse region. Moreover, the maximum IPCE value of $CuFe_2O_4/WO_3$ is 47.27% at 350 nm, which is 1.21 times higher than that of WO_3. As the number of electrons in the external circuit produced by an incident photon at a given wavelength divided by the number of incident photons, IPCE is determined by three microscopic processes: light harvesting (LH), separation of opposing charges (CS), and a collection of the charges (CC) at the electrodes. Considering the similar light absorbance of two samples as shown in Fig. 5, the different value of IPCE at the whole light response region indicates that the separation of opposing charges is the main factor. So the improvement of photoelectrochemical performance is ascribed to the presence of p-n heterojunction.

Based on the above results, a simple mechanism of the conduction and valence band positions for $CuFe_2O_4/WO_3$ is shown in Fig.11. The space charge region caused by p-n heterojunction has a beneficial effect of improving the charges separation [22]. In this way, photo-generated holes transfer to $CuFe_2O_4$, and more photo-generated electrons can transfer to conductive substrates without recombination. Therefore, it can be concluded that the p-n heterojunction promotes electron/hole separation, leading to an enhanced photoelectrochemical performance.

Conclusion

In summary, the $CuFe_2O_4/WO_3$ p-n heterojunction film was synthesized and deposited on the FTO substrate by a doctor-blade method and a deposition-annealing method. The results of TEM, SEM and XPS show that $CuFe_2O_4$ nanoparticles were deposited on the surface of WO_3 film. Mott–Schottky and electrochemical impedance spectroscopy analysis confirmed the formation of p–n heterojunction, and $CuFe_2O_4/WO_3$ heterojunction film shows an enhanced photoelectorchemical properties compared to WO_3 film. The presence of p-n heterojunction facilitates the separation of photoinduced electrons and holes, leading to more efficient charge transfer, resulting in a significant improvement in PEC performance.

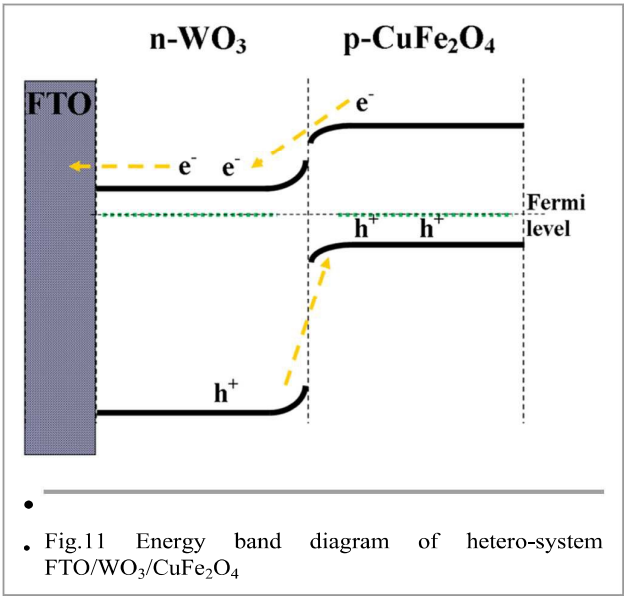

Fig.11 Energy band diagram of hetero-system $FTO/WO_3/CuFe_2O_4$

Acknowledgements

This study was supported by the National Nature Science Foundation of China (No. 51304253), the Fundamental Research Funds for the Central Universities of Central South University (2015zzts021), and Y.L. acknowleges financial support from the China Scholarship Council (CSC File No. 201406370157).

References

1. A. Fujishima and K. Honda, *Nature*, 1972, 238, 37-38.
2. K. P. S. Parmar, H. J. Kang, A. Bist, P. Dua, J. S. Jang and J. S. Lee, *ChemSusChem*, 2012, 5, 1926-1934.
3. T. M. Breault and B. M. Bartlett, *The Journal of Physical Chemistry C*, 2013, 117, 8611-8618.
4. Z.-F. Huang, J. Song, L. Pan, X. Zhang, L. Wang and J.-J. Zou, *Advanced Materials*, 2015, 27, 5309-5327.
5. T. Zhang, Z. Zhu, H. Chen, Y. Bai, S. Xiao, X. Zheng, Q. Xue and S. Yang, *Nanoscale*, 2015, 7, 2933-2940.
6. Y. Sun, C. J. Murphy, K. R. Reyes-Gil, E. A. Reyes-Garcia, J. M. Thornton, N. A. Morris and D. Raftery, *International Journal of Hydrogen Energy*, 2009, 34, 8476-8484.
7. Y. Liu, W. Li, J. Li, Y. Yang and Q. Chen, *RSC Advances*, 2014, 4, 3219-3225.
8. S. Ghosh, S. S. Acharyya, M. Kumar and R. Bal, *RSC Advances*, 2015, 5, 37610-37616.
9. A. Tanaka, K. Hashimoto and H. Kominami, *Journal of the American Chemical Society*, 2013,

136, 586-589.
10. B. Cole, B. Marsen, E. Miller, Y. Yan, B. To, K. Jones and M. Al-Jassim, *The Journal of Physical Chemistry C*, 2008, 112, 5213-5220.
11. Y. Liu, J. Li, W. Li, Y. Yang, Y. Li and Q. Chen, *The Journal of Physical Chemistry C*, 2015, 119, 14834-14842.
12. M. Khajeh Aminian and M. Hakimi, *Catalysis Science & Technology*, 2014, 4, 657-664.
13. L. Huang, H. Xu, Y. Li, H. Li, X. Cheng, J. Xia, Y. Xu and G. Cai, *Dalton Transactions*, 2013, 42, 8606-8616.
14. Z. Liu, Z.-G. Zhao and M. Miyauchi, *The Journal of Physical Chemistry C*, 2009, 113, 17132-17137.
15. J. Su, L. Guo, N. Bao and C. A. Grimes, *Nano Letters*, 2011, 11, 1928-1933.
16. Y. Liu, H. He, J. Li, W. Li, Y. Yang, Y. Li and Q. Chen, *RSC Advances*, 2015, 5, 46928-46934.
17. R. Saito, Y. Miseki and K. Sayama, *Chemical Communications*, 2012, 48, 3833-3835.
18. K. C. Leonard, K. M. Nam, H. C. Lee, S. H. Kang, H. S. Park and A. J. Bard, *The Journal of Physical Chemistry C*, 2013, 117, 15901-15910.
19. H. Yang, J. Yan, Z. Lu, X. Cheng and Y. Tang, *Journal of Alloys and Compounds*, 2009, 476, 715-719.
20. R. Ding, L. Lv, L. Qi, M. Jia and H. Wang, *RSC Advances*, 2014, 4, 1754-1760.
21. J. H. Kim, J. H. Kim, J.-W. Jang, J. Y. Kim, S. H. Choi, G. Magesh, J. Lee and J. S. Lee, *Advanced Energy Materials*, 2015, 5, n/a-n/a.
22. N. Nasrallah, M. Kebir, Z. Koudri and M. Trari, *Journal of Hazardous Materials*, 2011, 185, 1398-1404.
23. C. Karunakaran, S. SakthiRaadha, P. Gomathisankar and P. Vinayagamoorthy, *RSC Advances*, 2013, 3, 16728-16738.
24. A. Kezzim, N. Nasrallah, A. Abdi and M. Trari, *Energy Conversion and Management*, 2011, 52, 2800-2806.
25. M. Wang, L. Sun, J. Cai, P. Huang, Y. Su and C. Lin, *Journal of Materials Chemistry A*, 2013, 1, 12082-12087.
26. J. Cao, J. Xing, Y. Zhang, H. Tong, Y. Bi, T. Kako, M. Takeguchi and J. Ye, *Langmuir*, 2013, 29, 3116-3124.
27. L. J. Minggu, K. H. Ng, H. A. Kadir and M. B. Kassim, *Ceramics International*, 2014, 40, 16015-16021.
28. J. Hou, C. Yang, H. Cheng, S. Jiao, O. Takeda and H. Zhu, *Energy & Environmental Science*, 2014, 7, 3758-3768.
29. M. Wang, L. Sun, Z. Lin, J. Cai, K. Xie and C. Lin, *Energy & Environmental Science*, 2013, 6, 1211-1220.
30. Z. Kang, X. Yan, Y. Wang, Z. Bai, Y. Liu, Z. Zhang, P. Lin, X. Zhang, H. Yuan, X. Zhang and Y. Zhang, *Scientific Reports*, 2015, 5, 7882.
31. R. Rajendran, Z. Yaakob, M. A. Mat Teridi, M. S. Abd Rahaman and K. Sopian, *Materials Letters*, 2014, 133, 123-126.
32. A. Kargar, K. Sun, Y. Jing, C. Choi, H. Jeong, Y. Zhou, K. Madsen, P. Naughton, S. Jin, G. Y. Jung and D. Wang, *Nano Letters*, 2013, 13, 3017-3022.
33. J. A. Seabold, K. Shankar, R. H. T. Wilke, M. Paulose, O. K. Varghese, C. A. Grimes and K.-S. Choi, *Chemistry of Materials*, 2008, 20, 5266-5273.
34. G. Dai, J. Yu and G. Liu, *The Journal of Physical Chemistry C*, 2011, 115, 7339-7346.
35. Y. Liu, J. Li, W. Li, Q. Liu, Y. Yang, Y. Li and Q. Chen, *International Journal of Hydrogen Energy*, 2015, 40, 8856-8863.
36. S. Cong, Y. Tian, Q. Li, Z. Zhao and F. Geng, *Advanced Materials*, 2014, 26, 4260-4267.
37. Y. Zhao, G. He, W. Dai and H. Chen, *Industrial & Engineering Chemistry Research*, 2014, 53, 12566-12574.
38. C. Reitz, C. Suchomski, J. Haetge, T. Leichtweiss, Z. Jaglicic, I. Djerdj and T. Brezesinski, *Chemical Communications*, 2012, 48, 4471-4473.
39. M. M. Momeni and Y. Ghayeb, *Journal of Electroanalytical Chemistry*, 2015, 751, 43-48.
40. J. Zhu, W. Li, J. Li, Y. Li, H. Hu and Y. Yang, *Electrochimica Acta*, 2013, 112, 191-198.
41. Q. Liu, J. He, T. Yao, Z. Sun, W. Cheng, S. He, Y. Xie, Y. Peng, H. Cheng, Y. Sun, Y. Jiang, F. Hu, Z. Xie, W. Yan, Z. Pan, Z. Wu and S. Wei, *Nature Communications*, 2014, 5, 5122.
42. J. Schneider, M. Matsuoka, M. Takeuchi, J. Zhang, Y. Horiuchi, M. Anpo and D. W. Bahnemann, *Chemical Reviews*, 2014, 114, 9919-9986.
43. K. Zhang, X.-J. Shi, J. K. Kim and J. H. Park, *Physical Chemistry Chemical Physics*, 2012, 14, 11119-11124.
44. M. Ibadurrohman and K. Hellgardt, *International Journal of Hydrogen Energy*, 2014, 39, 18204-18215.
45. K. Chen, X. Feng, R. Hu, Y. Li, K. Xie, Y. Li and H. Gu, *Journal of Alloys and Compounds*, 2013, 554, 72-79.

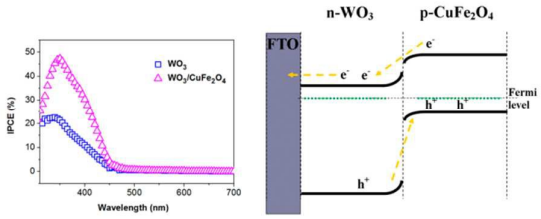

$CuFe_2O_4$ was loaded on the surface of WO_3 film to form p-n heterojunction photoanode with a better performance than WO_3.